

IMPERIAL

OPTIMAL CONTROL OF TRAPPED IONS

THE NOISE-RESILIENT ENTANGLING GATES

Author

ZHI ZENG

CID: 06015879

Supervised by

PROF. F. MINTERT

Self-Study Project of
Master of Science in Physics with Quantum Dynamics

Department of Physics
Imperial College London
2025

Abstract

Trapped ions are among the most promising platforms for practical quantum computing (QC). Scaling trapped-ion quantum processors to large sizes while simultaneously mitigating decoherence and control errors remains a major challenge on the path to fault-tolerant QC, as noise and fluctuations in experimental parameters inevitably become more pronounced with increasing system size. We review various noise-resilient schemes for entangling gates that build upon and extend the Mølmer-Sørensen (MS) gate, addressing different sources of infidelity. Beginning with a categorization of error mechanisms, we discuss four types of entangling gates, including the MS gate, its polychromatic variants, and gates specifically designed for general noise resilience and amplitude noise suppression.

Contents

Abstract	i
1 Infidelity in Trapped-Ion Quantum Gates	1
1.1 Introduction	1
1.2 The Errors Causing Infidelity	2
1.2.1 Coherent Errors	2
1.2.2 Incoherent Errors	3
2 The Standard Mølmer-Sørensen Gate	5
2.1 The Monochromatic Scheme	5
2.2 The Bichromatic Scheme	8
3 The Polychromatic Mølmer-Sørensen Gate	9
3.1 Theoretical Proposal	9
3.1.1 Dissipative Dynamics	10
3.1.2 Polychromatically Driven Gates	10
3.1.3 The Analysis of Infidelity	11
3.2 Experimental Demonstration	12
4 Generally Noise-resilient Entangling Gates	14
4.1 Hamiltonian Model	14
4.2 Driving Patterns	15
4.3 Numerical Results	17
5 Amplitude-noise-resilient Entangling Gates	20
5.1 The Sensitivity to Amplitude in Harmonic Trap	20
5.2 Numerical Exploration	21
5.3 Anharmonic Physics and Optimal Scheme	22
Conclusions	24
Bibliography	25

1

Infidelity in Trapped-Ion Quantum Gates

Contents

1.1 Introduction	1
1.2 The Errors Causing Infidelity	2
1.2.1 Coherent Errors	2
1.2.2 Incoherent Errors	3

1.1 Introduction

Constructing a quantum processor capable of tackling highly complex real-world problems necessitates not only a large-scale qubit system, but also precise and reliable gate operations [1]. The trapped-ion system, where ions are confined in radio-frequency (RF) Paul traps [2] and manipulated precisely using electromagnetic fields, stands out as one of the most promising systems for realizing such a quantum processor. In this system, ions serve as qubits, with carefully selected internal states representing $|0\rangle$ and $|1\rangle$, while entanglement is achieved by using shared vibrational modes as a quantum bus. Up to now, on trapped ion platforms, single-qubit gates [3, 4], two-qubit gates [5–7], and qubit state preparation and readout [8] have all been performed with fidelities exceeding that required for fault-tolerant quantum computing (QC) using high-threshold quantum error correction codes [9]. However, despite their promising capabilities, significant challenges remain in the pursuit of a practical quantum processor. Chief among these is scaling up the trapped-ion systems while maintaining the ability to individually control and measure them with high fidelity.

As systems scale towards large quantum processors, the level of noise and fluctuations in experimental parameters becomes increasingly significant. For instance, many proposed trapped-ion quantum processors will require ions to be confined

near the surface of a microfabricated chip [10–13], where voltage fluctuations in the electrodes induce motional heating and dephasing, posing challenges to maintaining coherence and gate fidelity.

Thus, the development of more robust gate operations is essential—ones that not only achieve low error rates under ideal conditions, but are also resilient in many-ion systems operating within realistic experimental environments.

In addition, achieving universal QC requires the implementation of a universal set of quantum gates, which consists of arbitrary single-qubit rotations and at least one kind of entangling two-qubit gates [14]. Among various two-qubit gates, the Mølmer-Sørensen (MS) gate has emerged as a leading candidate in trapped-ion QC due to its intrinsic ability to generate high-fidelity entanglement across multiple qubits [15, 16].

Thus, in this review, we will focus on various robust control schemes that build upon and extend the MS gate.

1.2 The Errors Causing Infidelity

The fidelity measuring the overlap between the ideal and the actual operation is defined as

$$F = \langle \psi_{\text{ideal}} | \rho_{\text{actual}} | \psi_{\text{ideal}} \rangle, \quad (1.1)$$

where $|\psi_{\text{ideal}}\rangle$ is the target state and ρ_{actual} is the state actually produced.

Then the infidelity is simply given by

$$I = 1 - F, \quad (1.2)$$

which quantifies how much a real quantum operation deviates from its ideal, error-free version. It encapsulates all sources of errors and their cumulative effects.

To achieve high-fidelity gate operations, it is crucial to identify the factors contributing to infidelity, allowing for targeted mitigation strategies. Here, based on the first principle, I introduce a hierarchical categorization of errors in the MS gate, organized into a first-level, second-level, and third-level structure. By their physical nature, the gate errors can be broadly categorized into coherent and incoherent errors. Coherent errors are those manifest as systematic, deterministic deviations in the unitary evolution of the system, while incoherent errors arise from stochastic processes that cause irreversible loss of quantum information.

1.2.1 Coherent Errors

As shown in Fig. 1.1, coherent errors are classified into systematic errors and deterministic classical control errors. Systematic errors are inherent to the system due to imperfect modeling or unwanted couplings, and they can be explicitly subdivided into theoretical approximation errors and crosstalk.

In the context of MS gate, the common analytical approximation errors arise from four sources: the effective Hamiltonian approximation, the Lamb-Dicke approximation (where the Lamb-Dicke parameter $\eta \ll 1$), the rotating wave approximation (RWA), and the truncation of the Magnus expansion. When the gate speed

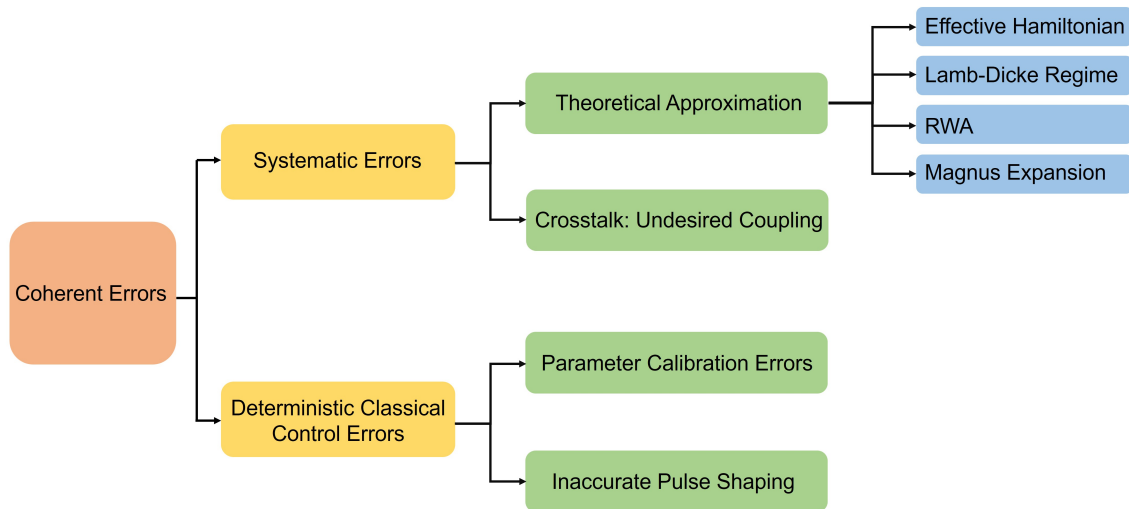


Figure 1.1: A hierarchical tree of coherent errors.

becomes too fast, off-resonant terms contribute non-negligibly, causing the RWA to break down, which in turn limits the achievable gate speed. Moreover, in some cases the system operates beyond the Lamb-Dicke regime—particularly when strong ion-motion interactions or higher motional states are involved. In such cases, the assumption of weak laser-ion coupling is no longer valid.

Crosstalk between ions[17], mainly the undesired coupling between qubits and non-targeted motional modes, will amplify noise sensitivity. It often becomes significant in many-ion systems with a complex multi-mode structure. This arises because the coupling strengths corresponding to different vibrational modes become comparable in magnitude and vary across different ions in the chain. In such systems, selectively driving a single mode unavoidably triggers higher-order phonon exchange processes, inadvertently coupling non-targeted spectator modes to the qubit states.

As for deterministic classical control errors, they often consist of inaccurate pulse shaping leading to phase and amplitude errors, and parameter calibration errors including fixed miscalibration of pulse durations, amplitudes, or detunings.

Thus, coherent errors are typically systematic and, in many cases, can be corrected with proper calibration or optimized pulse design.

1.2.2 Incoherent Errors

Similarly, as shown in Fig. 1.2, within the first-level classification of incoherent errors, decoherence effects and stochastic classical control errors are further categorized at the second level. This kind of errors arise from the environment or random control fluctuations, often setting a fundamental limit on gate fidelity.

The discussion of decoherence errors can be categorized into two distinct aspects: decoherence of the qubit state and decoherence of the motional state.

The qubit decoherence is characterized by two fundamental timescales: T_1 , the energy relaxation time, and T_2 , the phase coherence time. Energy relaxation results from coupling between the qubit and its environment, leading to population decay between the ground and excited states. For optical qubits, spontaneous photon

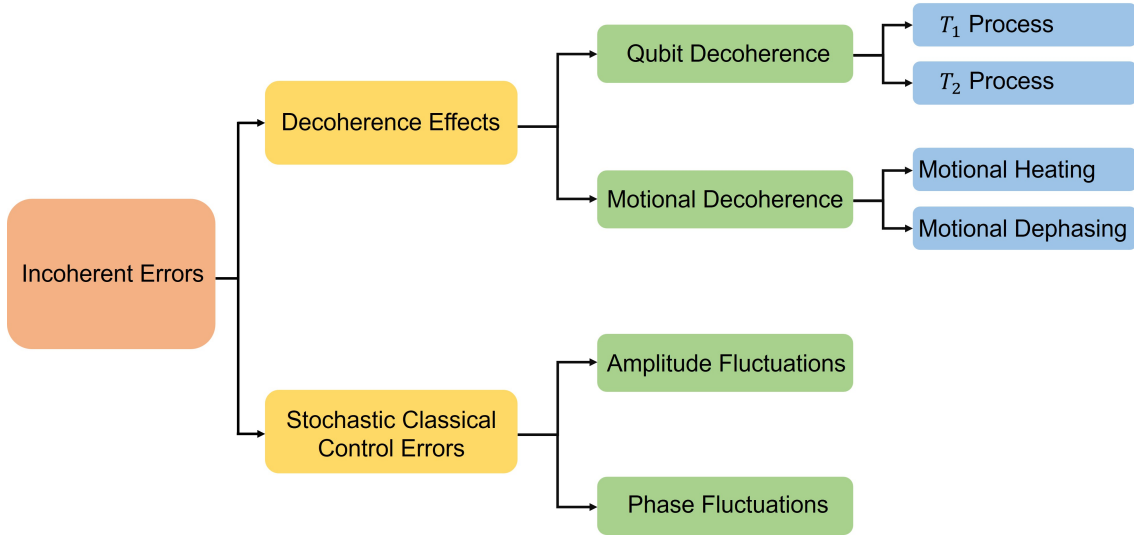


Figure 1.2: A hierarchical tree of incoherent errors.

emission and thermalization contribute to energy loss, whereas for hyperfine qubits, T_1 is effectively infinite on typical gate timescales due to the absence of spontaneous decay. Phase decoherence arises from fluctuations in the relative phase between the qubit's basis states due to environmental noise. The dominant physical sources include magnetic field fluctuations and laser phase noise. Basically, the decoherence of the qubit state for trapped ion platform is negligible due to its sufficient long internal-state coherence time.

In contrast, the decoherence of motional mode can severely impact the overall gate performance. This decoherence arises from two primary mechanisms: motional heating and motional dephasing. Motional heating occurs when the ion's motional state absorbs energy from environmental noise, leading to an increase in the average phonon number. The dominant sources include fluctuations in the trapping potential, ambient stray electric fields, and imperfections in the trap electrodes or power supplies. Motional dephasing is the loss of phase coherence in the motional state caused by variations in the RF drive, slow drifts or noise in control voltages, and mechanical vibrations or acoustic noise.

Stochastic classical control errors come from random fluctuations in control parameters, including amplitude and phase instabilities. These errors manifest as fluctuations in the intensity of control fields and phase jitter in laser or microwave fields.

To reiterate, rather than pursuing high fidelity by striving for ideal experimental conditions or minimizing external noise sources, the literature review discusses various gate control schemes that mitigate the sensitivity of gate performance to noise and experimental imperfections.

2

The Standard Mølmer-Sørensen Gate

Contents

2.1 The Monochromatic Scheme	5
2.2 The Bichromatic Scheme	8

Before the MS gate was proposed, the dominant source of quantum gate infidelity in trapped-ion QC architectures stemmed from the decoherence of quantum states, which occurred due to interactions between the environment and the quantum channel responsible for mediating logic operations between qubits [18].

In 1999, Mølmer and Sørensen introduced a quantum logic gate based on motional excitations that exhibits intrinsic resilience to such environmental interactions. Their scheme realizes a controlled-phase gate that does not require the ions to be prepared in the motional ground state [15], since the internal and motional degrees of freedom are completely disentangled for all phonon number states n . An additional feature of the MS interaction is its ability to generate entanglement among multiple ions using only globally applied laser fields. Unlike gate schemes that require individual addressing of ions with tightly focused laser beams, the MS interaction simplifies experimental implementation while maintaining high-fidelity entanglement generation.

2.1 The Monochromatic Scheme

In the monochromatic scheme, similar to the trapped-ion proposal by Cirac and Zoller [18], each ion is addressed with a single laser, but quantum logic gates are implemented by employing off-resonant laser pulses to mediate two-ion interactions. Rather than directly driving transitions between internal states, their scheme leverages a detuned virtual excitation of vibrational sidebands to achieve an effective

coupling between qubits. Specifically, as shown in Fig. 2.1(a), the laser applied to the first ion is detuned close to the upper motional sideband, meaning its frequency is near resonance with a transition that simultaneously excites both the internal and vibrational degrees of freedom of the ion. The laser applied to the second ion is set to a detuning equal in magnitude but opposite in sign to that of the first laser.

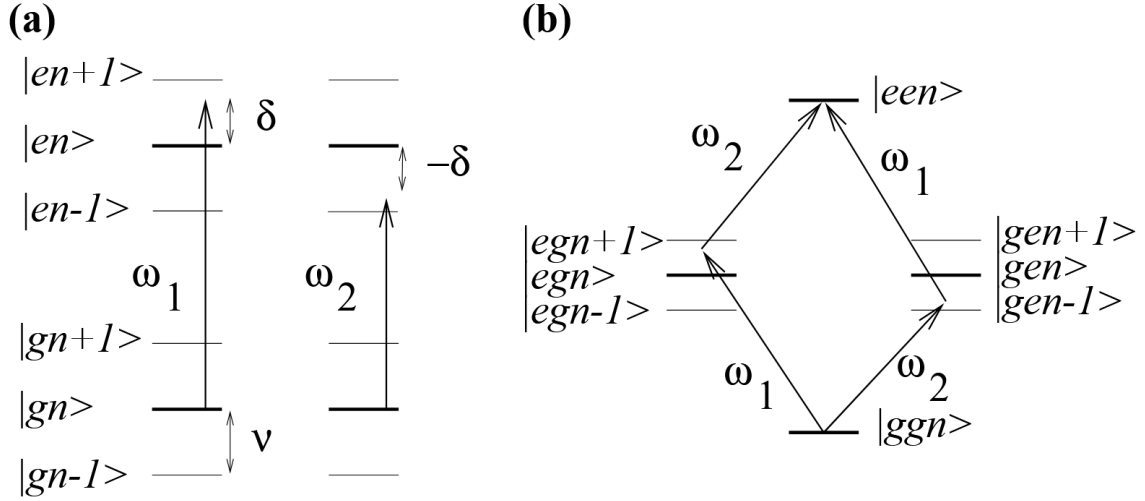


Figure 2.1: Schematic diagram for energy levels and laser drivings.

This configuration establishes an effective coupling between the states $|ggn\rangle$ and $|een\rangle$, where g and e denote the internal states of the ions and n represents the quantum number of the relevant motional mode. The detuning is chosen to be sufficiently large so that the intermediate states $|egn + 1\rangle$ and $|gen - 1\rangle$ remain unpopulated throughout the gate operation.

This ion-trapped system is described by:

$$\begin{aligned}
 H &= H_0 + H_{\text{int}} \\
 H_0 &= \hbar\nu (a^\dagger a + 1/2) + \hbar\omega_{eg} \sum_i \sigma_{zi}/2 \\
 H_{\text{int}} &= \sum_i \frac{\hbar\Omega_i}{2} \left(\sigma_{+i} e^{i(\eta_i(a+a^\dagger) - \omega_i t)} + h.c. \right),
 \end{aligned} \tag{2.1}$$

where ν is the collective frequency, a^\dagger (a) is the creation (annihilation) operator of the motional mode and $\hbar\omega_{eg}$ is the energy difference between the qubit states. η_i , Ω_i and ω_i are the Lamb-Dicke parameter, Rabi frequency and the laser frequency for the i -th ion.

The gate operates within the Lamb-Dicke regime, *i.e.* $\eta_i\sqrt{n+1}$ remains well below unity while this may still allow n well above unity. Assumptions include free selection of two ions from the ion string, and $\eta_1 = \eta_2 = \eta$, $\Omega_1 = \Omega_2 = \Omega$. By choosing the detunings as described earlier, the only energy conserving transitions occur between $|ggn\rangle$ and $|een\rangle$. The effective Rabi frequency $\tilde{\Omega}$ governing these transitions, via intermediate states m , can be derived using second order perturbation theory,

$$\left(\frac{\tilde{\Omega}}{2}\right)^2 = \frac{1}{\hbar^2} \left| \sum_m \frac{\langle een|H_{\text{int}}|m\rangle \langle m|H_{\text{int}}|gg n\rangle}{E_{gg n} - \hbar\omega_i - E_m} \right|^2. \quad (2.2)$$

If we restrict the summation to $|egn + 1\rangle$ and $|gen - 1\rangle$, we obtain

$$\tilde{\Omega} = -\frac{(\Omega\eta)^2}{2(\nu - \delta)}, \quad (2.3)$$

where $\delta = \omega_1 - \omega_{eg}$ represents the detuning of the laser that addresses the first ion.

Notably, Eq. (2.3) is independent of the motional quantum number n due to interference between the two distinct transition pathways illustrated in Fig. 2.1(b). The opposite detunings ensure that the denominators in Eq. (2.2) carry opposite signs, leading to a complete cancellation of the n -dependent terms when subtracted. As a result, the coherent evolution of the internal states is entirely decoupled from the vibrational quantum number.

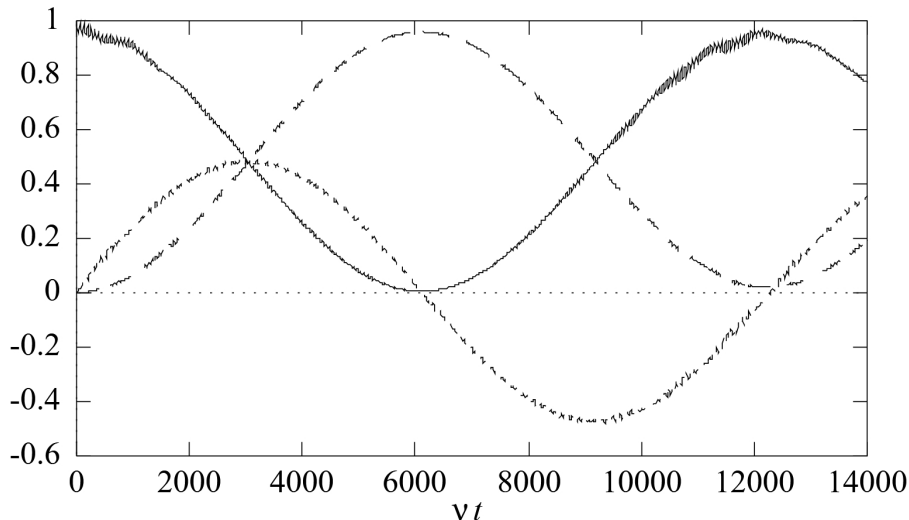


Figure 2.2: Rabi oscillations between $|gg\rangle$ and $|ee\rangle$, showing the time evolution of $\rho_{ee,ee}$ (long dashed line), $\rho_{gg,gg}$ (full line) and $\text{Im}(\rho_{gg,ee})$ (short dashed line). Initial states are the internal ground state and a $\bar{n} = 2$ coherent vibrational state. Parameters are $\eta = 0.10\nu$, $\delta = 0.90\nu$ and $\Omega = 0.10\nu$.

This perturbative analysis is verified numerically based on the exact Hamiltonian (2.1). These simulations are performed for various initial vibrational states, including Fock, coherent, and thermal states, while both ions are initially prepared in the internal ground state. And they all yield qualitatively consistent results. Fig. 2.2 gives the computational outcome for a coherent state of vibrational motion. The figure demonstrates that we have perfect Rabi oscillations between the internal states $|gg\rangle$ and $|ee\rangle$. Moreover, the values of the off-diagonal element $\rho_{gg,ee}$ indicate a coherent evolution of the internal atomic states that is disentangled from the vibrational motion throughout the process.

This scheme provides a framework for generating entanglement between the internal states, completely decoupled from the external vibrational mode. Starting from an initial state $\rho = |gg\rangle\langle gg| \otimes \rho_{vib}$, the radiation fields corresponding to a pulse

of duration $T = \frac{\pi}{2\Omega}$ can drive the system to $\rho = |\psi\rangle\langle\psi| \otimes \rho_{vib}$, where $|\psi\rangle$ represents a maximally entangled state $\frac{1}{\sqrt{2}}(|gg\rangle - i|ee\rangle)$.

It is also indicated by Eq. (2.3) that ions have no need to remain in a fixed vibrational state throughout the process. Thus, this scheme has inherent robustness against interaction with the environment, which is a key advantage of this scheme, since the heating of the vibrational mode contributes significantly to decoherence. As a result, the coherent oscillation between $|gg\rangle$ and $|ee\rangle$ may still exist even when the vibrational motion undergoes energy exchange with a thermal reservoir.

2.2 The Bichromatic Scheme

In the monochromatic scheme, the laser pulses will induce energy shifts in $|egn\rangle$ and $|gen\rangle$ that depend on n . These shifts introduce phase factors through time evolution, which can degrade the coherence between internal states. This issue can be addressed by a trick resembling photon echoes [19].

Instead of repeatedly inverting the detunings as in the photon echo technique, an alternative approach is to continuously apply laser fields with both detunings $\pm\delta$ on both ions. With two fields of opposite detunings and identical Rabi frequency Ω , two additional transition pathways contribute alongside those depicted in Fig. 2.1. These additional paths are identical in effect to the original ones, except for a modification in Eq. (2.3) by a factor of two. When bichromatic fields are employed, a resonant transition between $|eg\rangle$ and $|ge\rangle$ also emerges. The evolution is described by

$$\begin{aligned}
 |gg\rangle &\rightarrow \cos\left(\frac{\tilde{\Omega}T}{2}\right)|gg\rangle + i \sin\left(\frac{\tilde{\Omega}T}{2}\right)|ee\rangle \\
 |ee\rangle &\rightarrow \cos\left(\frac{\tilde{\Omega}T}{2}\right)|ee\rangle + i \sin\left(\frac{\tilde{\Omega}T}{2}\right)|gg\rangle \\
 |ge\rangle &\rightarrow \cos\left(\frac{\tilde{\Omega}T}{2}\right)|ge\rangle - i \sin\left(\frac{\tilde{\Omega}T}{2}\right)|eg\rangle \\
 |eg\rangle &\rightarrow \cos\left(\frac{\tilde{\Omega}T}{2}\right)|eg\rangle - i \sin\left(\frac{\tilde{\Omega}T}{2}\right)|ge\rangle.
 \end{aligned} \tag{2.4}$$

The robustness of Eq. (2.4) against motional heating is confirmed through numerical simulations incorporating a thermal reservoir.

Notably, in a system with only two trapped ions, the use of bichromatic laser fields leads to the evolution described by Eq.(2.4) without requiring individual optical addressing. And when the same field simultaneously illuminates multiple ions, it generates multi-particle entanglement [16].

3

The Polychromatic Mølmer-Sørensen Gate

Contents

3.1 Theoretical Proposal	9
3.1.1 Dissipative Dynamics	10
3.1.2 Polychromatically Driven Gates	10
3.1.3 The Analysis of Infidelity	11
3.2 Experimental Demonstration	12

Despite resilience to initial motional state, the standard MS gate remains susceptible to various errors, due to its intrinsic interactions with the environment, as well as systematic errors arising from imperfect calibration of system parameters. Thus, a new type of MS gate based on suitably chosen polychromatic driving is proposed [20, 21]. This multitone generalization of the MS (MTMS) gate not only protects against infidelity caused by heating of the motional mode and slow fluctuations and mis-sets in the trap frequency, but also relaxes ion cooling requirements.

3.1 Theoretical Proposal

The infidelity of quantum gates originates from the decoherence of the internal states, which is mainly due to the decoherence of the quantum bus mode during gate operation in the presence of noise. Since the MS gate ensures complete disentanglement between the internal states and the bus mode in the ideal coherent evolution, this connection of the decoherence between the internal states and the bus mode occurs via ion-phonon entanglement in the dissipative dynamics.

3.1.1 Dissipative Dynamics

The MS Hamiltonian can be written as

$$H(t) = (\Upsilon(t)a + \Upsilon^*(t)a^\dagger)S_x, \quad (3.1)$$

where $S_x = \sum_j \sigma_x^{(j)}$ and $\Upsilon(t) = \eta\Omega \exp(i\delta t)$ with the detuning δ . The propagator induced by $H(t)$ is expressed as

$$\mathcal{U}_K = \exp(-i((f(t)a + f^*(t)a^\dagger)S_x - g(t)S_x^2)), \quad (3.2)$$

with $f(t) = \int_0^t dt' \Upsilon(t')$ and $g(t) = \mathcal{I} \left[\int_0^t dt' \Upsilon(t') f^*(t') \right]$.

The MS evolution is governed solely by the spin-spin interaction term S_x^2 when f vanishes, leading to the dynamics independent of the motional state of the bus mode. However, incoherent processes during the gate operation still constitute a significant factor of infidelity. The term $(f(t)a + f^*(t)a^\dagger)S_x$ in equation (3.2) indicates that the dissipation of the ions' motion will affect the coherence of the qubits. The predominant effects—thermalization and dephasing—can be described by a master equation characterized by the following generator [22]

$$\mathcal{L}[\circ] = -i[H(t), \circ] + \sum_{j=+, -, d} \gamma_j \mathcal{D}_{E_j}[\circ]. \quad (3.3)$$

The first term describes unitary dynamics and the second term, the dissipator, consists of $\mathcal{D}_{\hat{O}}[\circ] = \hat{O} \circ \hat{O}^\dagger - \frac{1}{2}\{\hat{O}^\dagger \hat{O}, \circ\}$ with Lindblad operators $E_+ = a^\dagger$ and $E_- = a$ for thermalization and $E_d = a^\dagger a = \hat{n}$ for dephasing.

In the time-dependent frame defined by $\mathcal{U}_K(t)$, the ideal unitary evolution including the perfect entangling gate is transformed to the identity. In this interaction picture, the master equation simplifies, leaving only dissipative dynamics with a time-dependent dissipator $\tilde{\mathcal{L}}[\circ] = \sum_j \gamma_j \mathcal{D}_{\tilde{E}_j}[\circ]$ with

$$\begin{aligned} \tilde{E}_- &= a - i f^*(t) S_x, \\ \tilde{E}_+ &= a^\dagger + i f(t) S_x, \\ \tilde{E}_d &= \hat{n} + i(f(t)a - f^*(t)a^\dagger)S_x + |f(t)|^2 S_x^2. \end{aligned} \quad (3.4)$$

These Lindblad operators \tilde{E}_j include both qubits and motional operators, which explicitly reflect the influence of motional decoherence on the qubits throughout the gate operation.

3.1.2 Polychromatically Driven Gates

Since deviations from ideal gate operations result from ion-phonon entanglement, as characterized by $f(t)$ in equation (3.2), achieving high gate fidelities may require minimizing the deviations of $f(t)$ from 0. The best choice is to minimize $\langle |f^2| \rangle$ while enforcing the constraint $\langle f \rangle = 0$, where the expectation operator $\langle \cdot \rangle = \int_0^T dt \cdot$ represents time integration over the gate duration T .

To determine optimized control pulses, the laser field is expanded as the trun-

cated Fourier series

$$\Upsilon_p = \sum_{j=1}^m c_j \delta \exp(ij\delta t), \quad (3.5)$$

where c_j are dimensionless complex amplitudes and δ is the fundamental frequency. The requirement for $\mathcal{U}_{\mathcal{K}}(T)$ with $T = 2\pi/\delta$ to implement a maximally entangling gate $\exp(-i\frac{\pi}{8}S_x^2)$ is given by $\sum_j |c_j|^2/j = 1/16$, and the overall optimization is

$$\min_{c_j} \left(\sum_{j=1}^m \frac{|c_j|^2}{j^2} \mid \sum_{j=1}^m \frac{c_j}{j} = 0, \sum_{j=1}^m \frac{|c_j|^2}{j} = \frac{1}{16} \right). \quad (3.6)$$

The optimal coefficient c_j^{opt} is [23]

$$c_j^{opt} = \frac{j b}{1 - j\lambda} \text{ and } b = -\frac{1}{4} \left(\sum_{j=1}^m \frac{j}{(1 - j\lambda)^2} \right)^{-\frac{1}{2}}, \quad (3.7)$$

where λ is the smallest root of the equation

$$\sum_{j=1}^m (1 - j\lambda)^{-1} = 0. \quad (3.8)$$

As a result, rather than driving each ion sideband with a single field, MTMS gates apply N fields to drive each sideband at detunings $\delta_j = j\delta$ with $\{j = 1, \dots, N\}$ as illustrated in Fig. 3.1, The strength of each tone is given by coefficients c_j , which can be chosen to be real. The Hamiltonian thus becomes

$$H_{\text{MTMS}} = \delta\eta\Omega S_x \sum_{j=1}^N c_j (a e^{-ij\delta t} + a^\dagger e^{ij\delta t}). \quad (3.9)$$

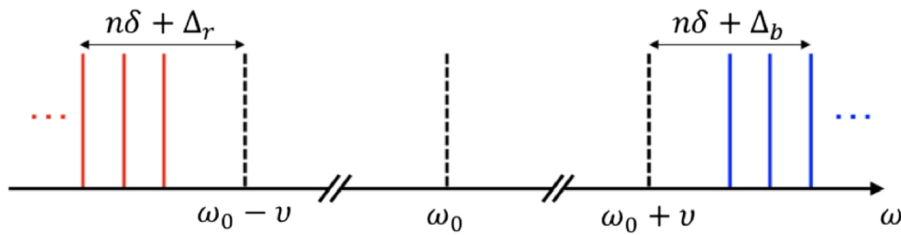


Figure 3.1: Energy level diagram showing multitone gate fields detuned from the correct gate detuning δ by Δ_r and Δ_b for the red and blue sidebands, respectively.

3.1.3 The Analysis of Infidelity

In practical implementations, a number of factors contribute to deviations from an idealized MS gate operation, leading to a reduction in gate fidelity. This discussion focuses on two primary sources of infidelity: phase decoherence induced by heating of the motional mode during gate operation, and symmetric detuning error results from an incorrect measurement of trap frequency.

If the total infidelity is small, the gate fidelity can be approximated as a sum of independent contributions $F = 1 - (E_h + E_\Delta + E_{oth})$, where E_h accounts for infidelity induced by motional heating, E_Δ represents the infidelity due to symmetric detuning error, and E_{oth} encapsulates all other sources of error, which are not considered further in this analysis. Since the infidelities are assumed to be small, only leading terms in the heating rate and detuning error are retained. Then, for the conventional MS gate, the errors introduced by nonzero heating rate and symmetric detuning error are given by

$$E_h = \frac{\pi \dot{n}}{\delta}, \quad E_\Delta = \left(\frac{3}{4} + \bar{n}\right) \pi^2 \left(\frac{\Delta}{\delta}\right)^2, \quad (3.10)$$

respectively, where \dot{n} is the heating rate and Δ is the error in gate detuning.

For the MTMS gate, the heating rate in E_h is rescaled by a factor given by

$$\dot{n}_{\text{MT}} = 8 \left(\sum_{j=1}^N \frac{c_j^2}{j^2} + \left(\sum_{j=1}^N \frac{c_j}{j} \right)^2 \right) \dot{n}. \quad (3.11)$$

For $N = \{1, 2, 3\}$, $\dot{n}_{\text{MT}} = \{1, 1/3, 1/5.19\} \times \dot{n}$, respectively. The optimization conditions lead to a smaller effective heating rate, meaning that the dephasing is less sensitive to heating rate.

Furthermore, the infidelity of the optimized MTMS gate due to symmetric detuning error, to leading order in Δ/δ , is expressed as

$$\begin{aligned} E_\Delta^{\text{MT}} &\approx 16\pi^2 \left(\frac{\Delta}{\delta}\right)^2 \left(\sum_{j=1}^N \frac{c_j^2}{j^2}\right)^2 \\ &= \frac{1}{36}\pi^2 \left(\frac{\Delta}{\delta}\right)^2 \approx 0.028\pi^2 \quad (N = 2) \\ &= \frac{39 - 12\sqrt{3}}{1936}\pi^2 \left(\frac{\Delta}{\delta}\right)^2 \approx 0.0094\pi^2 \quad (N = 3). \end{aligned} \quad (3.12)$$

Compared with Eq. (3.10), the sensitivity to Δ is reduced for two- and three-tone gates. Notably, this infidelity is also independent of the initial motional state distribution, unlike Eq. (3.10). The reason is that, at this order of Δ/δ , the residual ion-motional entanglement does not contribute to the infidelity, which is instead entirely attributed to the erroneous phase accumulation during the gate operation.

3.2 Experimental Demonstration

The above technique is experimentally demonstrated using a pair of $^{171}\text{Yb}^+$ ions [24]. To verify the effectiveness of the MTMS scheme in mitigating the impact of heating, the heating rate was artificially increased by introducing controlled noise. Fig. 3.2 shows the gate fidelity as a function of three distinct heating rates—the intrinsic heating rate with no added noise and two artificially enhanced heating rates—for both single- and two-tone gates.

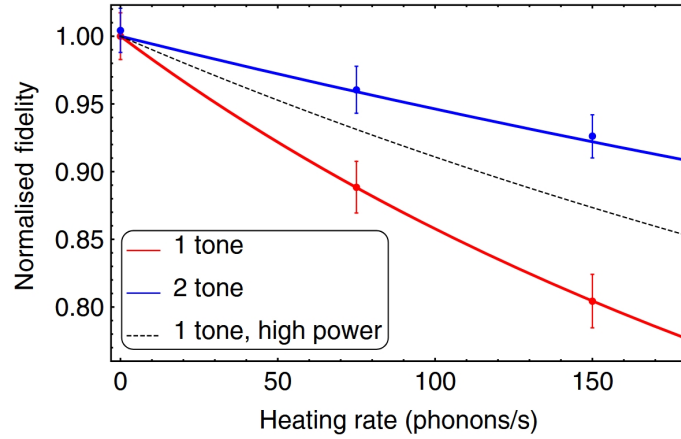


Figure 3.2: Infidelities resulting from heating are reduced by moving from a single- to a two-tone MS gate, shown in red and blue, respectively.

Solid lines are the results of a numerical simulation of the master equation with appropriate Lindblad operators to model heating effects, and three experimental points are shown for each type of gate. The dashed line corresponds to a simulation of a single-tone gate performed at a higher power, defined by the peak Rabi frequency used for the two-tone gate. The comparison shows that two-tone gates still exhibit lower error due to heating. In the absence of artificially induced heating, the two-tone gate does not show a fidelity enhancement over the single-tone gate, as the heating contribution to the overall infidelity is smaller than the experimental measurement uncertainty.

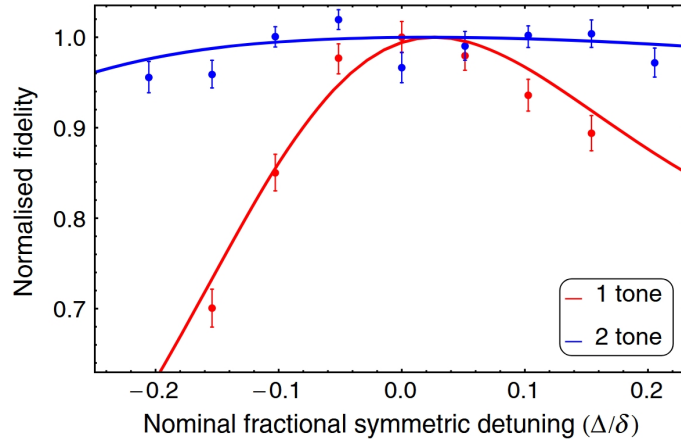


Figure 3.3: The effect of symmetric detuning error is significantly reduced by moving to two tones.

To demonstrate the resilience of MTMS gate against symmetric detuning errors, a symmetric detuning error of up to 0.2δ was added to the nominal zero error detuning. The results in Fig. 3.3 illustrate the dependence of fidelity on detuning errors, with solid lines showing the result of numerical simulations. Consistency between experimental data and simulation confirms the enhanced robustness of the two-tone gate compared to the conventional single-tone MS gate, demonstrating effective suppression of both heating-induced errors and detuning-related infidelities.

4

Generally Noise-resilient Entangling Gates

Contents

4.1 Hamiltonian Model	14
4.2 Driving Patterns	15
4.3 Numerical Results	17

The complex interplay of various error mechanisms in entangling gates poses a significant challenge for developing a robust scheme capable of mitigating multiple errors simultaneously. Although certain approaches have demonstrated enhanced resilience against specific noise sources, optimizing for one error mechanism often comes at the expense of another[17, 25]. These conflicting effects underscore the need for control protocols that can simultaneously address diverse error sources.

Based on an analysis of the primary error mechanisms in current implementations, a gate scheme is proposed that integrates multiple strategies to combat various error sources in trapped-ion QC [26]. This control framework enables high-fidelity entanglement in hot trapped ion chains with a multi-mode structure, demonstrating inherent resilience against motional heating as well as increased robustness against fluctuations in both normal-mode frequencies and qubit frequency.

4.1 Hamiltonian Model

The system consists of N ions and M collective motional modes is described by the Hamiltonian

$$H_0 = \sum_{j=1}^N \frac{\omega_j}{2} \sigma_z^{(j)} + \sum_{l=1}^M \nu_l a_l^\dagger a_l, \quad (4.1)$$

where ω_j is the resonance frequency for ion j , and $\nu_l = \kappa_l \nu$ is the resonant frequency for motional mode in terms of the trapping frequency ν .

The interaction with an external light field can excite both internal states and motional states. The corresponding interaction Hamiltonian takes the form

$$H(t) = \sum_{j=1}^N f_j(t) \sigma_+^{(j)} \prod_{l=1}^M e^{i\eta_{jl}(a_l + a_l^\dagger)} + h.c., \quad (4.2)$$

where $\sigma_+^{(j)}$ is the raising operator and $f_j(t)$ is the driving functions encapsulating the generally time-dependent Rabi frequency as well as a time-dependence due to carrier frequencies of the light field.

Since entanglement is achieved via the exchange of virtual phonons in the motional mode, the interaction Hamiltonian can be expressed in terms of the operators

$$\mathcal{D}_{l,k}(\eta) = \sum_{n=0}^{\infty} (i\eta)^{2n+k} \frac{a_l^{\dagger n+k} a_l^n}{(n+k)!n!}, \quad \mathcal{D}_{l,-k}(\eta) = (-1)^k \mathcal{D}_{l,k}^\dagger(\eta) \quad (4.3)$$

for $k \geq 0$, that encapsulate all processes involving the creation and annihilation of k phonons in a given mode l , *i.e.*, they capture the k -th order sideband transitions of the motional mode l .

By transforming to the interaction picture and applying RWA, the renormalised driving patterns can be generally parameterized as

$$\tilde{f}_j(t) = -i \sum_l \frac{1}{\eta_{jl}} \sum_k F_{l,k}^{(j)}(t) e^{-i(k\nu_l + \omega_j)t}, \quad (4.4)$$

where the exponential factors $e^{-i(k\nu_l + \omega_j)t}$ capture the time dependence required to achieve resonance with a specific sideband transition. The factors $F_{l,k}^{(j)}(t)$ vary slowly with time compared to ν_l and account for finite detuning and temporal modulation that can be used to achieve the desired robustness. The requirement for a coherent gate indicates that the driving amplitude follows the relation $F_{l,-k}^{(j)} = (-1)^k (F_{l,k}^{(j)})^*$.

With such driving patterns, the interaction Hamiltonian reduces to

$$H(t) = \sum_{j=1}^N \sigma_y^{(j)} \sum_{l,k>0} \frac{F_{l,k}^{(j)}(t)}{\eta_{jl}} \mathcal{D}_{l,k} \prod_{l' \neq l} \mathcal{D}_{l',0} + h.c.. \quad (4.5)$$

4.2 Driving Patterns

By carefully selecting the driving functions $F_{l,k}^{(j)}(t)$, the ion-field interaction can be tailored to induce specific entanglement. For the MS gate, entanglement is achieved by exclusively driving the first sideband of selected motional modes [15, 27], which requires weak coupling or motional states near ground states as this allows the displacement operators in Eq. (4.5) to be approximated to the lowest order in η . Beyond the Lamb-Dicke regime, alternative strategies are required to maintain high-fidelity gate operations.

Stronger ion-motion interactions or higher motional excitations necessitate considering higher-order phonon-exchange processes in Eq. (4.3), which introduces more complex spin-motion interactions and indirect couplings between driven and spectator modes, requiring control schemes accounting not only for higher-order phonon processes but also for the phonon exchange processes in the non-addressed vibrational modes. To address these challenges, high-fidelity entangling gates for many-mode ion chains beyond the Lamb-Dicke regime require a higher-order expansion of the interaction Hamiltonian $H(t)$, involving selecting a suitable set of driven vibrational modes L and optimized sideband choices $K(L)$.

In a system with M motional modes, the proposed gate scheme simultaneously drives all modes ($L = M$). The first-order sideband ($k = 1$) of a specific central mode, typically chosen for its stronger spin-motion coupling, serves as the primary entangling channel, while second-order sidebands ($k = 2$) across all modes suppress unwanted higher-order contributions.

With such choice, the Hamiltonian (4.5) simplifies to

$$H_c(t) = \sum_{j=1}^N \sigma_y^{(j)} \left(\frac{F_{1,1}^{(j)}(t)}{\eta_{j1}} \mathcal{D}_{1,1} \mathcal{D}_1 + \sum_{l=1}^M \frac{F_{l,2}^{(j)}(t)}{\eta_{jl}} \mathcal{D}_{l,2} \mathcal{D}_l \right) + h.c., \quad (4.6)$$

where $\mathcal{D}_l = \prod_{l' \neq l} \mathcal{D}_{l',0}$ is the product of phonon-conserving operators in spectator modes.

From Eq. (4.6), tailored driving functions $F_{1,1}^{(j)}$ and $F_{l,2}^{(j)}$ can be derived to exactly capture the driven dynamics up to a particular order of η . While higher-order solutions are theoretically feasible, the present scheme employs an expansion up to $\mathcal{O}(\eta^3)$, significantly refining first-order approximations while minimizing the number of required sidebands. The driving functions are given by

$$F_{1,1}^{(1)} = F_{1,1}^{(2)} = \Omega \left(e^{2i\delta t} - \frac{3}{2} e^{3i\delta t} \right), \quad (4.7a)$$

$$F_{l,2}^{(1)} = \text{sign}(\eta_{1l}) \Omega \frac{\tilde{\eta}_l}{\eta_{1l}} e^{i\delta t}, \quad (4.7b)$$

$$F_{l,2}^{(2)} = \text{sign}(\eta_{2l}) \Omega \frac{\tilde{\eta}_l}{\eta_{2l}} e^{i\delta t}, \quad (4.7c)$$

where $\tilde{\eta}_l := \frac{\sqrt{5}}{2} \sqrt{\eta_{1l}^2 + \eta_{2l}^2}$.

Fig. 4.1 illustrates the driving processes applied to a selected ion pair within an N -ion chain. According to Eq. (4.7a), both ions experience identical bichromatic modulation with detunings 2δ and 3δ , targeting the first sideband of the primary motional mode. This modulation enhances resilience against motional heating while the specific detuning ratio optimizes the gate speed. In addition, Eqs. (4.7b) and (4.7c) specify different drivings for each ion in the pair, targeting second-order sidebands of all motional modes. These tailored drivings suppress unwanted processes that arise as higher-order contributions to the system's dynamics and incorporate mode-dependent amplitudes to compensate for the different coupling strengths across different modes.

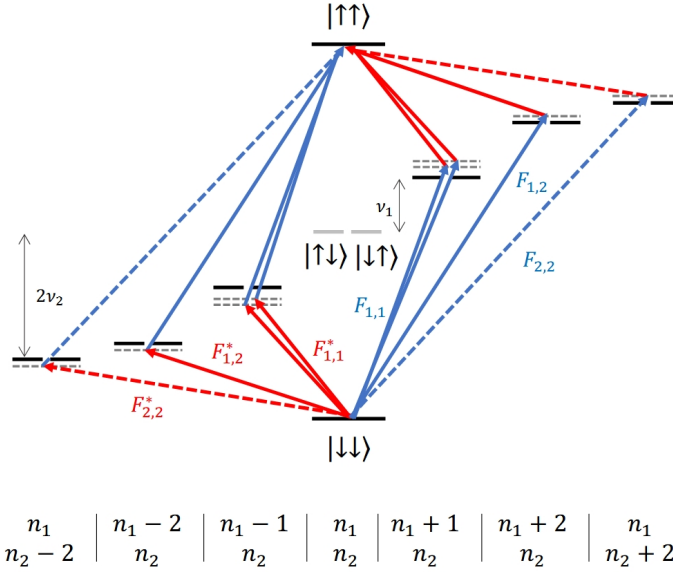


Figure 4.1: Energy level for two ions and two vibrational modes. Solid red (blue) sidebands represent transitions with a phonon loss (gain) in vibrational mode 1. Dashed red (blue) sidebands represent the same processes for vibrational mode 2.

4.3 Numerical Results

The proposed control scheme achieves high-fidelity entangling gates for trapped ions in the presence of noise, multiple collective motional modes, and high motional excitations.

Numerical simulations evaluate the fidelity F as a function of several key parameters, including chain size N , initial motional occupations $|n\rangle$, motional heating, and experimental imperfections like frequency errors in the motional modes ϵ_ν and spin transitions ϵ_ω .

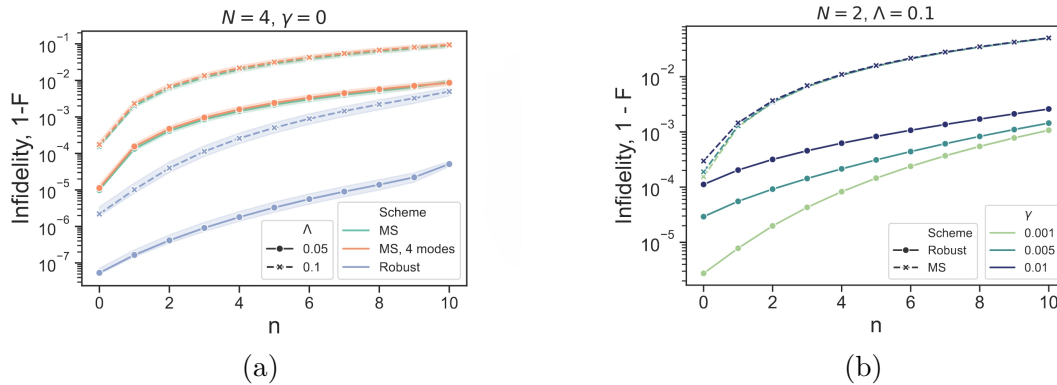


Figure 4.2: Infidelity $1-F$ of different schemes versus the initial Fock state occupation n for a 4-qubit (left panel) and 2-qubit (right panel) systems.

As shown in Fig. 4.2(a), the infidelity $1 - F$ of gates in a 4-ion system with no dissipation or frequency errors is depicted. The x -axis represents the initial motional Fock state $|n\rangle^{\otimes 4}$, while the shaded area shows the range of infidelities across all ion

pairs, with marker points denoting the average value. Different colors distinguish the present gate (blue), the standard MS gate applied to the center-of-mass (COM) mode (green), and the MS gate applied to all four motional modes [28] (orange), while varying marker styles correspond to different coupling strengths Λ .

Notably, under ideal conditions, the present gate consistently surpasses both MS implementations across all initial states and coupling regimes. This advantage is particularly pronounced in the weak-coupling regimes ($\Lambda = 0.05$, circles), where it achieves infidelities below 10^{-4} even at high motional excitations ($n = 10$).

Fig. 4.2(b) illustrates the performance of the proposed gate under motional heating in a two-ion system. Unlike the previous scenario, the coupling strength remains uniform across all vibrational modes and ions, allowing the local drivings to be relaxed to global ones. The plot shows the gate infidelity $1-F$ as a function of the motional occupation for a fixed coupling strength $\Lambda = 0.1$ and varying heating decay rates γ . Crosses represent the standard MS gate applied to the COM mode, while circles correspond to solutions derived from the parametrization in Eq. (4.7). The results demonstrate a significant advantage of the proposed strategy over the MS gate, particularly in low-dissipation environments. The enhanced robustness achieved through bichromatic driving enables fidelities close to 10^{-3} for motional occupations up to $n = 10$ in low-to-moderate dissipation ($\gamma \leq 0.01$), whereas the MS gate exhibits an infidelity around 10^{-1} .

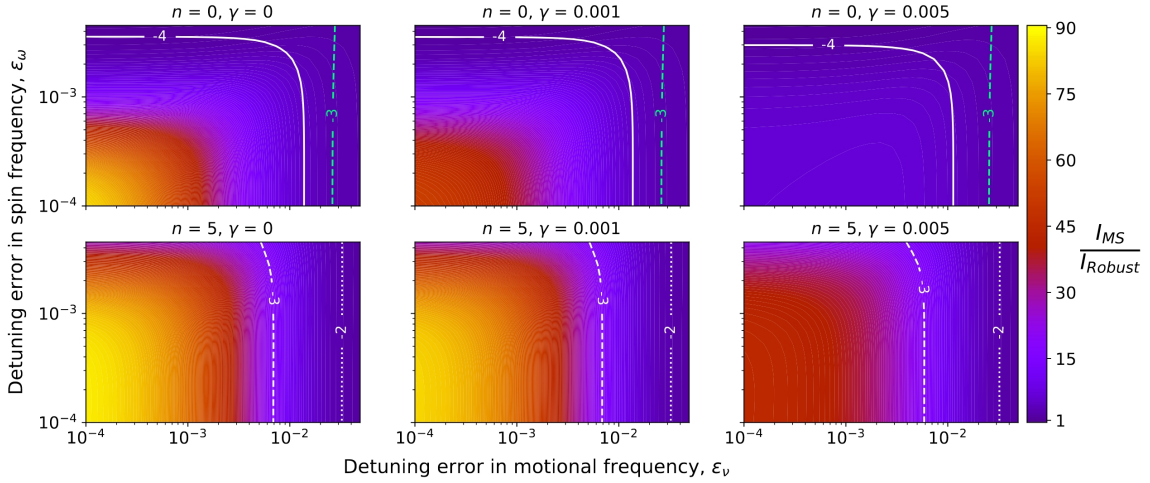


Figure 4.3: Combined impact of vibrational and spin frequency errors on the performance of the present entangling scheme (Robust) compared to the standard MS gate in a two-ion system.

Fig. 4.3 further examines the combined impact of detuning errors in vibrational and spin frequencies also under motional heating. Each panel represents the ratio of infidelities between the MS gate and the proposed robust scheme, I_{MS}/I_{Robust} , with colors ranging from purple (similar performance) to yellow (significant improvement). The panels vary across different initial motional states $|n\rangle$ and decay rates γ , while the x and y axes indicate detuning errors in vibrational ϵ_ν and spin frequencies ϵ_ω , respectively.

For an initial motional ground state, This robust scheme reduces infidelity by up to two orders of magnitude for small frequency errors, and even under motional

heating, it consistently outperforms the MS gate. with motional frequency errors limited to 1.5%, the robust gate achieves fidelities above 99.99%—improving performance by at least a factor of five—and maintains high fidelities (above 99%) even at higher motional excitations ($n \sim 100$) and broader error ranges, whereas the MS gate fails to reach 99% fidelity under any of the studied conditions.

5

Amplitude-noise-resilient Entangling Gates

Contents

5.1 The Sensitivity to Amplitude in Harmonic Trap	20
5.2 Numerical Exploration	21
5.3 Anharmonic Physics and Optimal Scheme	22

Resilience of entangling gates against a variety of errors can be achieved through suitably tailored temporal shapes of the driving fields [20, 21, 26, 29–31], except for fluctuations of the amplitude of driving field, which is tricky to achieve noise resilience against. The linear spatial dynamics of trapped ions inherently conflicts with the requirement for resilience against such amplitude variations. This required non-linearity can be obtained from the intrinsically non-linear light-matter interaction [32] beyond the Lamb-Dicke regime. Alternatively, anharmonicity in the trapping potential offers a way to achieve the desired robustness without requiring strong driving to induce significant non-linearity.

Although such anharmonicity will reduce resilience to thermal excitations, this effect can be mitigated through an appropriate choice of the temporal profile of the driving fields. This chapter introduces a gate scheme that achieves robustness against amplitude fluctuations by leveraging a weakly anharmonic trapping potential [33].

5.1 The Sensitivity to Amplitude in Harmonic Trap

Starting from the MS Hamiltonian of a pair of trapped ions:

$$H(t) = H_0 + \Omega_R(f(t)a^\dagger + f^*(t)a)S_x, \quad (5.1)$$

where $S_x = \sigma_x^1 + \sigma_x^2$, Ω_R is the Rabi frequency, and the function $f(t)$ encapsulates both the temporal modulation of the driving field carrier frequencies and any pulse-shaping-induced time dependence.

For an ideal harmonic bus mode, the influence of the non-interacting term H_0 reduces to an oscillatory evolution of a and a^\dagger . Thus the system Hamiltonian transforming to the interaction picture takes the form $\tilde{H}(t) = \Omega_R(\tilde{f}(t)a^\dagger + \tilde{f}^*(t)a)S_x$ with a driving function $\tilde{f}(t)$ incorporates the intrinsic time evolution of the non-interacting terms. The resulting gate dynamics corresponds to a phase-space trajectory, which is a closed loop with length proportional to Ω_R [15, 27]. The Rabi-angle Φ_R of the effective S_x^2 -interaction in this dynamics is proportional to the area enclosed by the loop, exhibiting the quadratic relation [31]

$$\Phi_R = \Omega_R^2 \operatorname{Im} \int_0^T d\tau \tilde{f}(\tau) \int_0^\tau d\tau' \tilde{f}^*(\tau'). \quad (5.2)$$

The dependence of Φ_R on the driving protocol factorizes into an amplitude term Ω_R^2 and a term determined by the specific temporal structure of the driving field. Since no choice of modulation $f(t)$ can alter this quadratic dependence on Rabi frequency, any fluctuation of Ω_R will inevitably lead to first-order variations in the Rabi-angle Φ_R .

However, for an anharmonic bus mode, the interplay between the interaction and the non-interacting terms can break this factorization, allowing for tailored driving patterns $f(t)$ that achieve resilience against fluctuations in the Rabi frequency Ω_R .

While anharmonicity can arise from any higher-order potential terms, the discussion here focuses on a quartic potential, $\frac{1}{2}m\omega^2(z^2 + z^4/\xi^2)$, where ξ represents the anharmonic length scale. The resulting perturbative correction to the COM mode's eigenfrequencies, induced by the anharmonicity, is given by $\chi n(n-1)$ with the phonon number n and the scalar prefactor

$$\chi = \frac{3\hbar}{4m\xi^2}. \quad (5.3)$$

5.2 Numerical Exploration

Fig. 5.1(a) illustrates the infidelity $1-F$ as a function of the Rabi frequency Ω_R for several gates. The solid red curve corresponds to a perfectly harmonic system, where no intrinsic resilience is achieved, leading to a rapid increase in infidelity as Ω_R deviates from its ideal value Ω_C . In contrast, the other two curves correspond to an anharmonic system, demonstrating the improved fidelities achieved by optimizing the driving patterns for a range of Rabi frequencies spanning $[9/10 \Omega_C, 11/10 \Omega_C]$. The pulses are optimised under the constraint $|f(t)| \leq 1$.

A more quantitative measure of robustness is given by the average infidelity I . Fig. 5.1(b) and (c) present I as a function of the central Rabi frequency Ω_C and the anharmonicity parameter χ for initial states with 0 phonons and up to 10 phonons, respectively. As expected, when anharmonicity is negligible, the infidelity remains relatively high. However, as χ increases, the infidelity decreases, ultimately reaching the threshold of 10^{-4} in the strong anharmonicity regime.

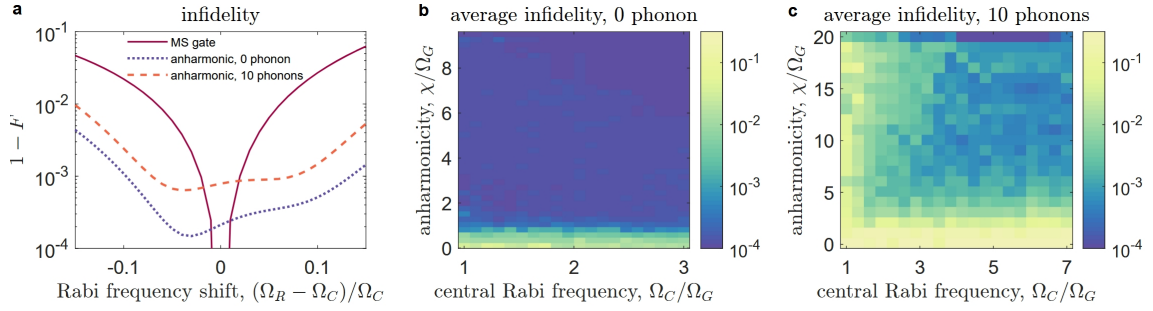


Figure 5.1: (a) Infidelity as a function of Rabi frequency's variation for the MS gate (solid red), the anharmonic gate without phonon excitation (dotted blue, for $\Omega_C = \Omega_G$, $\chi = 2\Omega_G$), and with 10 phonon excitations (dashed orange, for $\Omega_C = 2.6\Omega_G$, $\chi = 10\Omega_G$). (b) Infidelity averaged over a 10% error range of the Rabi frequency for no phonon excitation and (c) up to 10 phonon excitations, plotted against the anharmonicity and central Rabi frequency. The optimization process terminates once the infidelity falls below 10^{-4} .

While an ideal Rabi frequency $\Omega_R = \Omega_G$ suffices for achieving a fully entangling gate in the absence of amplitude fluctuations, Fig. 5.1(b) and (c) also indicate that achieving noise resilience may require slightly larger Rabi frequencies, depending on the targeted gate fidelity.

5.3 Anharmonic Physics and Optimal Scheme

To gain insight into the mechanism underlying the robustness against fluctuations in the Rabi frequency Ω_R , it is instructive to pursue an approximate treatment valid in the regime of strong anharmonicity. A gate acting on an initial motional state within the subspace spanned by the lowest N Fock states requires a tailored driving profile with components $g_n(t)$ close-to-resonant with transitions between adjacent Fock states. Under such conditions, after transforming into the interaction picture and applying RWA, the system Hamiltonian takes the form

$$H_I = \Omega_R \sum_{n=1}^N \sqrt{n} (g_n(t)\sigma_n^\dagger + g_n^*(t)\sigma_n) S_y, \quad (5.4)$$

with $\sigma_n = |n-1\rangle\langle n|$.

If the evolution operator V governing the qubit and motional dynamics satisfies

$$V(\mathbf{1} \otimes P) = \exp\left(-i\frac{\pi}{2} \sum_{n=1}^N n Z_n\right) (\mathbf{1} \otimes P), \quad (5.5)$$

where $Z_n = \frac{1}{4}[\sigma_n^\dagger, \sigma_n] S_y^2$, then the desired gate for initial motional states in the subspace $P = \sum_{n=1}^{N-1} |n\rangle\langle n|$ is achieved, thereby minimizing the infidelity I .

A practical choice for each of these driving functions $g_n(t)$ that ensures the desired robustness against amplitude noise is a piecewise-constant modulation with four segments, denoted as g_j , defined over time intervals $(j-1)T/4 \leq t < jT/4$ [34].

The explicit form of this modulation is given by

$$\begin{aligned} g_1 = g_4^* &= \frac{2\pi i}{\sqrt{n}\Omega_C T} \exp\left(-i\frac{3\phi}{4}\right), \\ g_2 = g_3^* &= \frac{2\pi i}{\sqrt{n}\Omega_C T} \exp\left(-i\frac{\phi}{4}\right). \end{aligned} \tag{5.6}$$

Given a central Rabi frequency with the value Ω_C , this driving pattern induces an effective gate operation of the form $\exp(i\phi Z_n)$ at the final time T . Fluctuations in Ω_R contribute only quadratically to the gate angle, that is, the gate is resilient to amplitude fluctuations up to second order, leading to robustness in the gate fidelity up to fourth order.

Conclusions

This work reviews various noise-resilient entangling gate schemes in trapped-ion quantum computing, focusing on four types of entangling gates: the standard MS gate, the MTMS gate, generally noise-resilient gates, and gates specifically designed for robustness against amplitude noise.

The standard MS gate is inherently insensitive to decoherence prior to the gate operation but remains vulnerable during the gate operation. The MTMS gate mitigates errors arising from motional heating and incorrect measurement of trap frequency. The generally noise-resilient entangling gate scheme demonstrates robustness against motional heating, spin and vibrational frequency errors and achieves high fidelity in hot trapped ion chain with complex multi-mode structure. The amplitude-noise-resilient gate significantly reduces the sensitivity of the Rabi angle to Rabi frequency fluctuations, suppressing its impact from first-order to quadratic dependence.

By systematically categorizing error sources, this work may be helpful for the development of more refined control strategies for mitigating a broader range of noise mechanisms, paving the way for high-fidelity entangling operations in large-scale trapped-ion quantum processors.

Bibliography

- [1] Colin D. Bruzewicz et al. “Trapped-ion quantum computing: Progress and challenges.” en. In: *Applied Physics Reviews* 6.2 (June 2019), p. 021314. ISSN: 1931-9401. DOI: [10.1063/1.5088164](https://doi.org/10.1063/1.5088164). URL: <https://pubs.aip.org/apr/article/6/2/021314/570103/Trapped-ion-quantum-computing-Progress-and> (visited on 02/27/2025).
- [2] W. Neuhauser et al. “Localized visible Ba + mono-ion oscillator.” In: *Phys. Rev. A* 22.3 (Sept. 1, 1980), pp. 1137–1140. ISSN: 0556-2791. DOI: [10.1103/PhysRevA.22.1137](https://doi.org/10.1103/PhysRevA.22.1137). URL: <https://link.aps.org/doi/10.1103/PhysRevA.22.1137> (visited on 02/27/2025).
- [3] K. R. Brown et al. “Single-qubit-gate error below 10^{-4} in a trapped ion.” In: *Phys. Rev. A* 84.3 (Sept. 14, 2011), p. 030303. ISSN: 1050-2947, 1094-1622. DOI: [10.1103/PhysRevA.84.030303](https://doi.org/10.1103/PhysRevA.84.030303). URL: <https://link.aps.org/doi/10.1103/PhysRevA.84.030303> (visited on 02/27/2025).
- [4] T. P. Harty et al. “High-Fidelity Preparation, Gates, Memory, and Readout of a Trapped-Ion Quantum Bit.” In: *Phys. Rev. Lett.* 113.22 (Nov. 24, 2014), p. 220501. ISSN: 0031-9007, 1079-7114. DOI: [10.1103/PhysRevLett.113.220501](https://doi.org/10.1103/PhysRevLett.113.220501). URL: <https://link.aps.org/doi/10.1103/PhysRevLett.113.220501> (visited on 02/13/2025).
- [5] Jan Benhelm et al. “Towards fault-tolerant quantum computing with trapped ions.” In: *Nature Physics* 4 (Apr. 2008). DOI: [10.1038/nphys961](https://doi.org/10.1038/nphys961).
- [6] J. P. Gaebler et al. “High-Fidelity Universal Gate Set for Be 9^{+} Ion Qubits.” In: *Phys. Rev. Lett.* 117.6 (Aug. 4, 2016), p. 060505. ISSN: 0031-9007, 1079-7114. DOI: [10.1103/PhysRevLett.117.060505](https://doi.org/10.1103/PhysRevLett.117.060505). URL: <https://link.aps.org/doi/10.1103/PhysRevLett.117.060505> (visited on 02/13/2025).
- [7] C. J. Ballance et al. “High-Fidelity Quantum Logic Gates Using Trapped-Ion Hyperfine Qubits.” In: *Phys. Rev. Lett.* 117.6 (Aug. 4, 2016), p. 060504. ISSN: 0031-9007, 1079-7114. DOI: [10.1103/PhysRevLett.117.060504](https://doi.org/10.1103/PhysRevLett.117.060504). URL: <https://link.aps.org/doi/10.1103/PhysRevLett.117.060504> (visited on 02/13/2025).
- [8] A. H. Myerson et al. “High-Fidelity Readout of Trapped-Ion Qubits.” In: *Phys. Rev. Lett.* 100.20 (May 23, 2008), p. 200502. ISSN: 0031-9007, 1079-7114. DOI: [10.1103/PhysRevLett.100.200502](https://doi.org/10.1103/PhysRevLett.100.200502). URL: <https://link.aps.org/doi/10.1103/PhysRevLett.100.200502> (visited on 02/27/2025).
- [9] Robert Raussendorf and Jim Harrington. “Fault-Tolerant Quantum Computation with High Threshold in Two Dimensions.” In: *Phys. Rev. Lett.* 98.19 (May 11, 2007), p. 190504. ISSN: 0031-9007, 1079-7114. DOI: [10.1103/PhysRevLett.98.190504](https://doi.org/10.1103/PhysRevLett.98.190504). URL: <https://link.aps.org/doi/10.1103/PhysRevLett.98.190504> (visited on 02/27/2025).

-
- [10] D. Kielpinski, C. Monroe, and D. J. Wineland. “Architecture for a large-scale ion-trap quantum computer.” In: *Nature* 417.6890 (June 2002), pp. 709–711. ISSN: 0028-0836, 1476-4687. DOI: [10.1038/nature00784](https://doi.org/10.1038/nature00784). URL: <https://www.nature.com/articles/nature00784> (visited on 02/27/2025).
- [11] C. Monroe et al. “Large-scale modular quantum-computer architecture with atomic memory and photonic interconnects.” In: *Phys. Rev. A* 89.2 (Feb. 13, 2014), p. 022317. ISSN: 1050-2947, 1094-1622. DOI: [10.1103/PhysRevA.89.022317](https://doi.org/10.1103/PhysRevA.89.022317). URL: <https://link.aps.org/doi/10.1103/PhysRevA.89.022317> (visited on 02/27/2025).
- [12] Bjoern Lekitsch et al. “Blueprint for a microwave trapped ion quantum computer.” In: *Sci. Adv.* 3.2 (Feb. 3, 2017), e1601540. ISSN: 2375-2548. DOI: [10.1126/sciadv.1601540](https://doi.org/10.1126/sciadv.1601540). URL: <https://www.science.org/doi/10.1126/sciadv.1601540> (visited on 02/27/2025).
- [13] A. Bermudez et al. “Assessing the Progress of Trapped-Ion Processors Towards Fault-Tolerant Quantum Computation.” In: *Phys. Rev. X* 7.4 (Dec. 13, 2017), p. 041061. ISSN: 2160-3308. DOI: [10.1103/PhysRevX.7.041061](https://doi.org/10.1103/PhysRevX.7.041061). URL: <https://link.aps.org/doi/10.1103/PhysRevX.7.041061> (visited on 02/27/2025).
- [14] Adriano Barenco et al. “Elementary gates for quantum computation.” In: *Phys. Rev. A* 52.5 (Nov. 1, 1995), pp. 3457–3467. ISSN: 1050-2947, 1094-1622. DOI: [10.1103/PhysRevA.52.3457](https://doi.org/10.1103/PhysRevA.52.3457). URL: <https://link.aps.org/doi/10.1103/PhysRevA.52.3457> (visited on 03/05/2025).
- [15] Anders Sørensen and Klaus Mølmer. “Quantum Computation with Ions in Thermal Motion.” In: *Phys. Rev. Lett.* 82.9 (Mar. 1, 1999), pp. 1971–1974. ISSN: 0031-9007, 1079-7114. DOI: [10.1103/PhysRevLett.82.1971](https://doi.org/10.1103/PhysRevLett.82.1971). URL: <https://link.aps.org/doi/10.1103/PhysRevLett.82.1971> (visited on 02/13/2025).
- [16] Klaus Mølmer and Anders Sørensen. “Multiparticle Entanglement of Hot Trapped Ions.” In: *Phys. Rev. Lett.* 82.9 (Mar. 1, 1999), pp. 1835–1838. ISSN: 0031-9007, 1079-7114. DOI: [10.1103/PhysRevLett.82.1835](https://doi.org/10.1103/PhysRevLett.82.1835). URL: <https://link.aps.org/doi/10.1103/PhysRevLett.82.1835> (visited on 03/05/2025).
- [17] Yao Lu et al. “Global entangling gates on arbitrary ion qubits.” In: *Nature* 572.7769 (Aug. 2019), pp. 363–367. ISSN: 0028-0836, 1476-4687. DOI: [10.1038/s41586-019-1428-4](https://doi.org/10.1038/s41586-019-1428-4). URL: <https://www.nature.com/articles/s41586-019-1428-4> (visited on 02/27/2025).
- [18] J. I. Cirac and P. Zoller. “Quantum Computations with Cold Trapped Ions.” In: *Phys. Rev. Lett.* 74.20 (May 15, 1995), pp. 4091–4094. ISSN: 0031-9007, 1079-7114. DOI: [10.1103/PhysRevLett.74.4091](https://doi.org/10.1103/PhysRevLett.74.4091). URL: <https://link.aps.org/doi/10.1103/PhysRevLett.74.4091> (visited on 03/05/2025).
- [19] S Zienau. “Optical Resonance and Two Level Atoms.” In: *Physics Bulletin* 26.12 (Dec. 1975), p. 545. DOI: [10.1088/0031-9112/26/12/039](https://doi.org/10.1088/0031-9112/26/12/039). URL: <https://dx.doi.org/10.1088/0031-9112/26/12/039>.

-
- [20] Farhang Haddadfarshi and Florian Mintert. “High fidelity quantum gates of trapped ions in the presence of motional heating.” In: *New J. Phys.* 18.12 (Dec. 2, 2016), p. 123007. ISSN: 1367-2630. DOI: [10.1088/1367-2630/18/12/123007](https://doi.org/10.1088/1367-2630/18/12/123007). URL: <https://iopscience.iop.org/article/10.1088/1367-2630/18/12/123007> (visited on 02/13/2025).
- [21] A. E. Webb et al. “Resilient Entangling Gates for Trapped Ions.” In: *Phys. Rev. Lett.* 121.18 (Nov. 1, 2018), p. 180501. ISSN: 0031-9007, 1079-7114. DOI: [10.1103/PhysRevLett.121.180501](https://doi.org/10.1103/PhysRevLett.121.180501). URL: <https://link.aps.org/doi/10.1103/PhysRevLett.121.180501> (visited on 02/13/2025).
- [22] G. Lindblad. “On the generators of quantum dynamical semigroups.” In: *Commun.Math. Phys.* 48.2 (June 1976), pp. 119–130. ISSN: 0010-3616, 1432-0916. DOI: [10.1007/BF01608499](https://doi.org/10.1007/BF01608499). URL: <http://link.springer.com/10.1007/BF01608499> (visited on 02/13/2025).
- [23] Albert Verdeny et al. “Optimal Control of Effective Hamiltonians.” In: *Phys. Rev. Lett.* 113.1 (July 2, 2014), p. 010501. ISSN: 0031-9007, 1079-7114. DOI: [10.1103/PhysRevLett.113.010501](https://doi.org/10.1103/PhysRevLett.113.010501). URL: <https://link.aps.org/doi/10.1103/PhysRevLett.113.010501> (visited on 02/13/2025).
- [24] James J. McLoughlin et al. “Versatile ytterbium ion trap experiment for operation of scalable ion-trap chips with motional heating and transition-frequency measurements.” In: *Phys. Rev. A* 83.1 (Jan. 21, 2011), p. 013406. ISSN: 1050-2947, 1094-1622. DOI: [10.1103/PhysRevA.83.013406](https://doi.org/10.1103/PhysRevA.83.013406). URL: <https://link.aps.org/doi/10.1103/PhysRevA.83.013406> (visited on 03/05/2025).
- [25] T. Choi et al. “Optimal Quantum Control of Multimode Couplings between Trapped Ion Qubits for Scalable Entanglement.” In: *Phys. Rev. Lett.* 112 (19 May 2014), p. 190502. DOI: [10.1103/PhysRevLett.112.190502](https://doi.org/10.1103/PhysRevLett.112.190502). URL: <https://link.aps.org/doi/10.1103/PhysRevLett.112.190502>.
- [26] Modesto Orozco-Ruiz, Wasim Rehman, and Florian Mintert. *Generally noise-resilient quantum gates for trapped-ions*. Apr. 19, 2024. DOI: [10.48550/arXiv.2404.12961](https://doi.org/10.48550/arXiv.2404.12961). arXiv: [2404.12961](https://arxiv.org/abs/2404.12961) [quant-ph]. URL: <http://arxiv.org/abs/2404.12961> (visited on 02/13/2025).
- [27] Anders Sørensen and Klaus Mølmer. “Entanglement and quantum computation with ions in thermal motion.” In: *Phys. Rev. A* 62.2 (July 18, 2000), p. 022311. ISSN: 1050-2947, 1094-1622. DOI: [10.1103/PhysRevA.62.022311](https://doi.org/10.1103/PhysRevA.62.022311). URL: <https://link.aps.org/doi/10.1103/PhysRevA.62.022311> (visited on 02/13/2025).
- [28] C. A. Sackett et al. “Experimental entanglement of four particles.” In: *Nature* 404.6775 (Mar. 2000), pp. 256–259. ISSN: 0028-0836, 1476-4687. DOI: [10.1038/35005011](https://doi.org/10.1038/35005011). URL: <https://www.nature.com/articles/35005011> (visited on 03/06/2025).
- [29] Alistair R. Milne et al. “Phase-Modulated Entangling Gates Robust to Static and Time-Varying Errors.” In: *Phys. Rev. Appl.* 13 (2 Feb. 2020), p. 024022. DOI: [10.1103/PhysRevApplied.13.024022](https://doi.org/10.1103/PhysRevApplied.13.024022). URL: <https://link.aps.org/doi/10.1103/PhysRevApplied.13.024022>.

- [30] A. Bermudez et al. “Robust trapped-ion quantum logic gates by continuous dynamical decoupling.” In: *Phys. Rev. A* 85 (4 Apr. 2012), p. 040302. DOI: [10.1103/PhysRevA.85.040302](https://doi.org/10.1103/PhysRevA.85.040302). URL: <https://link.aps.org/doi/10.1103/PhysRevA.85.040302>.
- [31] Jake Lishman and Florian Mintert. “Trapped-ion entangling gates robust against qubit frequency errors.” In: *Phys. Rev. Res.* 2 (3 July 2020), p. 033117. DOI: [10.1103/PhysRevResearch.2.033117](https://doi.org/10.1103/PhysRevResearch.2.033117). URL: <https://link.aps.org/doi/10.1103/PhysRevResearch.2.033117>.
- [32] Yotam Shapira et al. “Robust Two-Qubit Gates for Trapped Ions Using Spin-Dependent Squeezing.” In: *Phys. Rev. Lett.* 130 (3 Jan. 2023), p. 030602. DOI: [10.1103/PhysRevLett.130.030602](https://doi.org/10.1103/PhysRevLett.130.030602). URL: <https://link.aps.org/doi/10.1103/PhysRevLett.130.030602>.
- [33] Nguyen H. Le et al. *Amplitude-noise-resilient entangling gates for trapped ions*. July 3, 2024. DOI: [10.48550/arXiv.2407.03047](https://doi.org/10.48550/arXiv.2407.03047). arXiv: [2407.03047](https://arxiv.org/abs/2407.03047) [quant-ph]. URL: <http://arxiv.org/abs/2407.03047> (visited on 02/13/2025).
- [34] Holly K. Cummins, Gavin Llewellyn, and Jonathan A. Jones. “Tackling systematic errors in quantum logic gates with composite rotations.” In: *Phys. Rev. A* 67 (4 Apr. 2003), p. 042308. DOI: [10.1103/PhysRevA.67.042308](https://doi.org/10.1103/PhysRevA.67.042308). URL: <https://link.aps.org/doi/10.1103/PhysRevA.67.042308>.